# Mechanistic insights into enhanced photocatalytic $H_2O_2$ production induced by a Z-scheme heterojunction of copper bismuth oxide and molybdenum sulfide

*Akshay Tikoo[a], Nikitha Lohia[a], Sri Surya Charan Kondeti[a], Praveen Meduri [a*]*

[a] Department of Chemical Engineering, Indian Institute of Technology Hyderabad, Kandi,

Sangareddy-502285, Telangana (India)

**\* Corresponding Author**

Email: meduripraveen@che.iith.ac.in, Tel: 040-23016214

## Supplementary Information

1. $H_2O_2$ production using various photocatalysts

**Table S1.** $H_2O_2$ yield using different photocatalysts and sacrificial agents.

| Photocatalyst | Sacrificial reagent | Concentration (mg ml$^{-1}$) | $H_2O_2$ yield (µM h$^{-1}$) | Reference |
|---|---|---|---|---|
| Au-TiO$_2$ | HCOOH | 1 | 700 | [1] |
| Co@TiO$_2$ | CH$_3$OH | 1 | 1700 | [2] |
| CQDs@TiO$_2$ | C$_2$H$_5$OH | 1.33 | 1140 | [3] |
| CoP/g-C$_3$N$_4$ | C$_2$H$_5$OH | 1 | 70 | [4] |
| Nv- g-C$_3$N$_4$ | C$_2$H$_5$OH | 1 | 880 | [5] |
| RGO/Cd$_3$(TMT)$_2$ | CH$_3$OH | 4 | 292 | [6] |
| MIL-125-NH$_2$ | Benzylalcohol | 0.71 | 800 | [7] |
| Ov-Bi/Bi$_2$O$_{2-x}$CO$_3$ | C$_2$H$_5$OH | 4 | 400 | [8] |
| M-CdS | 2- propanol | 1 | 963 | [9] |

| | | | | |
|---|---|---|---|---|
| Au-MoS$_2$ | ----- | 1 | 132 | [10] |
| Fe$_2$O$_3$@C@1T/2H-MoS$_2$ | CH$_3$OH | 0.2 | 315 | [11] |

2. Crystallite size calculation

Scherrer's equation used to calculate the crystalline size is as follows:

$$D = K\lambda/\beta\cos(\theta) \qquad (i)$$

where  K is a dimensionless shape factor $= 0.9$;

$\lambda$ is x-ray wavelength;

$\beta$ is the full width at half maximum of the peak under consideration;

$\theta$ is the diffraction angle of the peak under consideration.

3. d-spacing calculation

The interplanar distance is calculated using the following equation:

$$d = n\lambda/2\sin(\theta) \qquad (ii)$$

where n is the order of diffraction;

$\lambda$ is the x-ray wavelength;

$\theta$ is the diffraction angle of the peak under consideration.

4. Tauc Plot
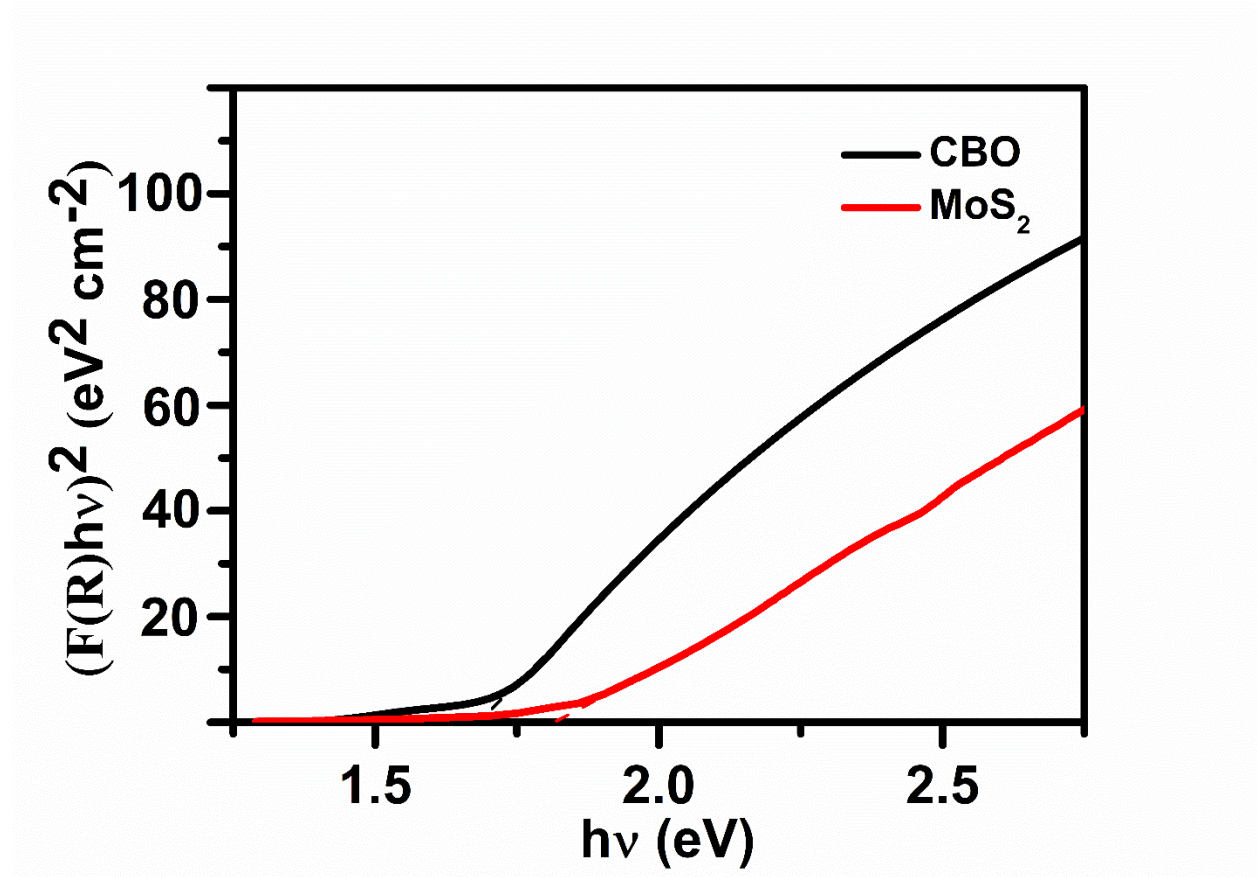


**Fig. S1.** Tauc plot of CBO and MoS$_2$.

Equation (iii) shows the relation between Kubelka-Munk function and band gap. The equation indicates that the intercept of the graph above is equal to the material band gap.

$$(F(R)h\nu)^2 = A(h\nu - E_g) \qquad \text{(iii)}$$

where  F(R) is Kubelka-Munk function;

h is the Planck's constant;

$\nu$ is the photons frequency;

A is a constant that depends on the transition probability;

$E_g$ is the bandgap.

**Table S2**. Bandgap of CBO and $MoS_2$.

| Sample | CBO | $MoS_2$ |
|---|---|---|
| Bandgap (eV) | 1.66 | 1.83 |
| CB (eV) | -0.6 | 0.12 |
| VB(eV) | 1.06 | 1.95 |

Valence band edge (VB) and conduction band edge (CB) of the materials are calculated using the following equations:

$$E_{VB} = \chi - E_e + 0.5E_g \qquad \text{(iv)}$$

$$E_{CB} = E_{VB} - E_g \qquad \text{(v)}$$

where $\chi$ is the absolute electronegativity;

$E_e$ is the energy of free electron on the normal hydrogen scale (4.5 eV);

$E_g$ is the bandgap.

5. TRPL spectroscopy

TRPL is used to understand the charge recombination. Decay curves are fitted by Edinburgh instrument's fluoracle software based on the exponential equation:

$$y = A + B_1 \exp(-t_1/\tau_1) + B_2 \exp(-t_2/\tau_2) + B_3 \exp(-t_3/\tau_3) \qquad \text{(vi)}$$

Average lifetime is calculated as follows:

$$\langle \tau \rangle = (B_1\tau_1^2 + B_2\tau_2^2 + B_3\tau_3^2)/(B_1\tau_1 + B_2\tau_2 + B_3\tau_3) \qquad \text{(vii)}$$

Time constants are tabulated below in Table S1.

**Table S3**. TRPL parameters

| Sample | $\tau_1$ (ns) | $\tau_2$ (ns) | $\tau_3$ (ns) | $\tau$ (ns) |
|---|---|---|---|---|
| CBO | 1.58 | 1.12 | 3.88 | 1.60 |
| $MoS_2$ | 2.79 | 1.44 | 8.81 | 2.85 |
| CBO@$MoS_2$ | 5.26 | 1.23 | 11.59 | 5.34 |

## 6. Electrochemical impedance spectroscopy (EIS)
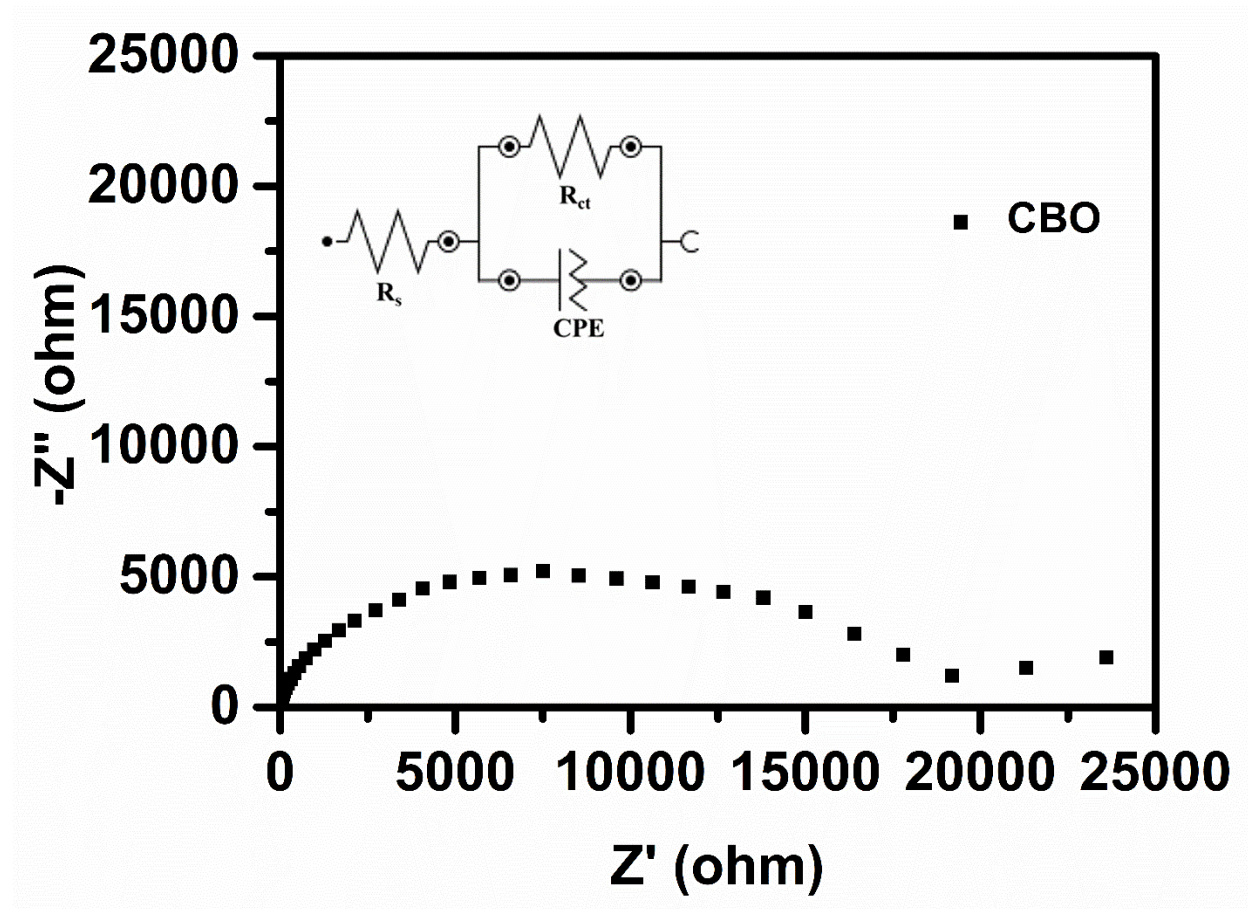


**Fig. S2.** EIS spectra of CBO.

**Table S4.** Fitted parameters for the circuit in Fig. S3

| Sample | CBO | $MoS_2$ | $CBO@MoS_2$ |
|---|---|---|---|
| $R_s$ (ohm) | 34.8 | 31.7 | 33.4 |
| $R_{ct}$ (kohm) | 20.6 | 5.9 | 3.8 |

7. Absorption curves for $H_2O_2$ production
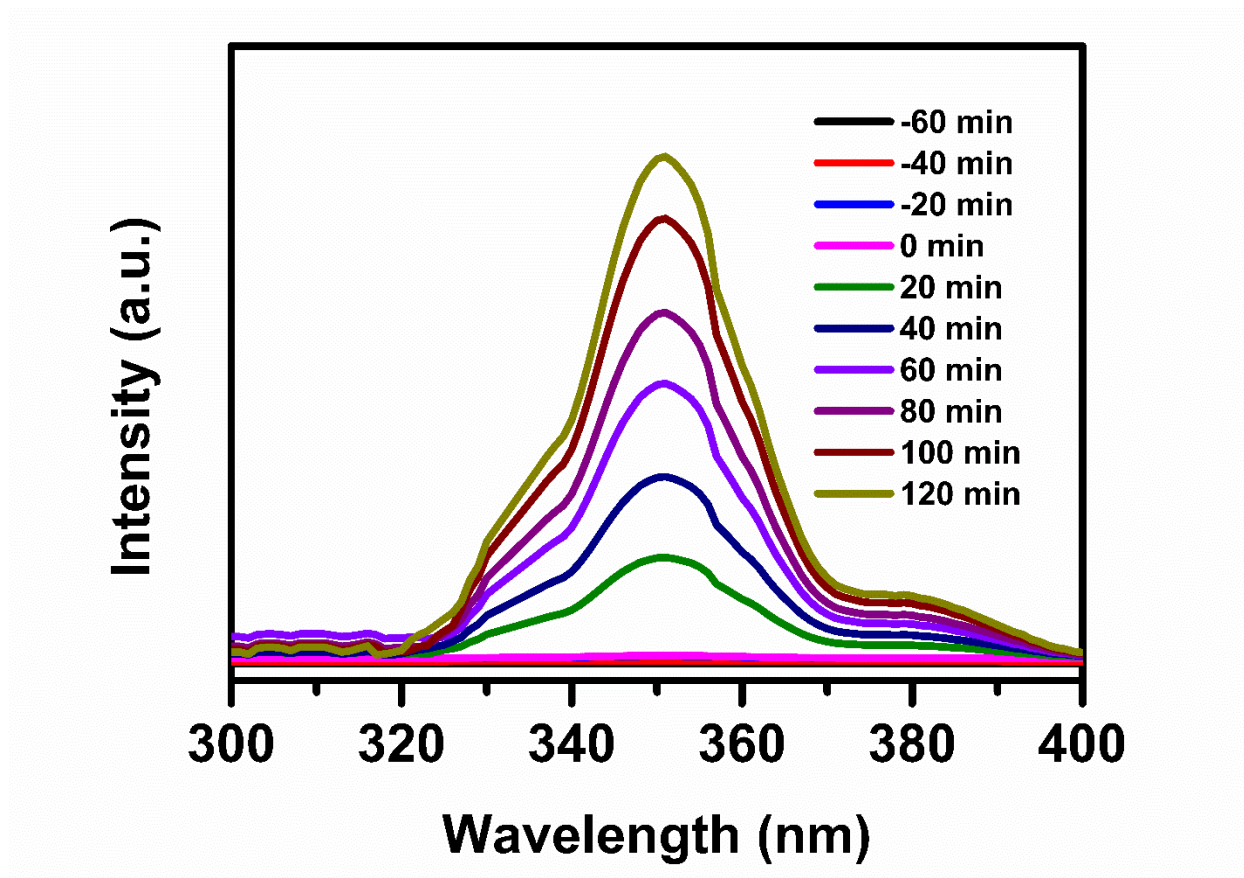


**Fig. S3.** Absorption curves for $H_2O_2$ production using CBO@MoS$_2$.

8. Material optimization
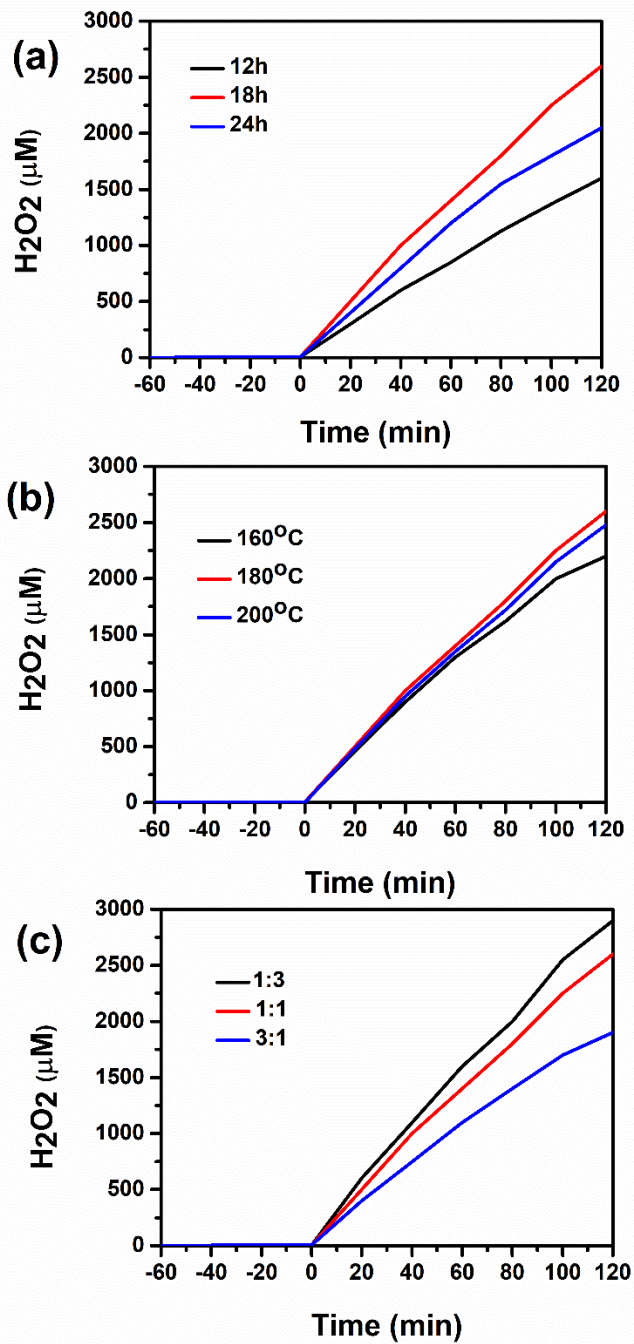


**Fig. S4.** $H_2O_2$ production with: (a) time of reaction. (b) temperature of reaction. (c) Ratio of

CBO and Mo precursor.

9. Kinetic modelling

**Table S5.** Rate constants and saturation concentration for $H_2O_2$ production.

| Sample | CBO | $MoS_2$ | CBO@MoS$_2$ |
|---|---|---|---|
| $K_f$ ($\mu$M min$^{-1}$) | 1.4 | 4.2 | 29.8 |
| $k_d$ (min$^{-1}$) | 0.011 | 0.0026 | 0.0036 |
| Saturation concentration ($\mu$M) | 130 | 1562 | 8372 |

**Table S6.** Rate constants and saturation concentration for $H_2O_2$ production using CBO@MoS$_2$.

| pH | 3 | 5 | 7 | 9 | 11 |
|---|---|---|---|---|---|
| $K_f$ ($\mu$M min$^{-1}$) | 37.2 | 31.7 | 29.8 | 26.5 | 23.1 |
| $k_d$ (min$^{-1}$) | 0.0028 | 0.0024 | 0.0036 | 0.0032 | 0.0033 |
| Saturation concentration ($\mu$M) | 13214 | 13345 | 8372 | 8337 | 7100 |

10. Solar to chemical conversion efficiency

**Table S7.** SCC efficiency.

| Sample | CBO | MoS$_2$ | CBO@MoS$_2$ |
|--------|-----|---------|-------------|
| Efficiency (%) | 0.02 | 0.7 | 0.37 |

SCC is determined using the following formula:

$$\text{SCC} = \frac{n * \Delta G^o}{P * A * T} * 100\% \qquad (x)$$

where n is number of moles of H$_2$O$_2$ produced;

$\Delta G^o$ is standard Gibbs free energy of the reaction;

P is power of light source;

A is illumination area;

T is time of reaction.

11. Scavenger effects
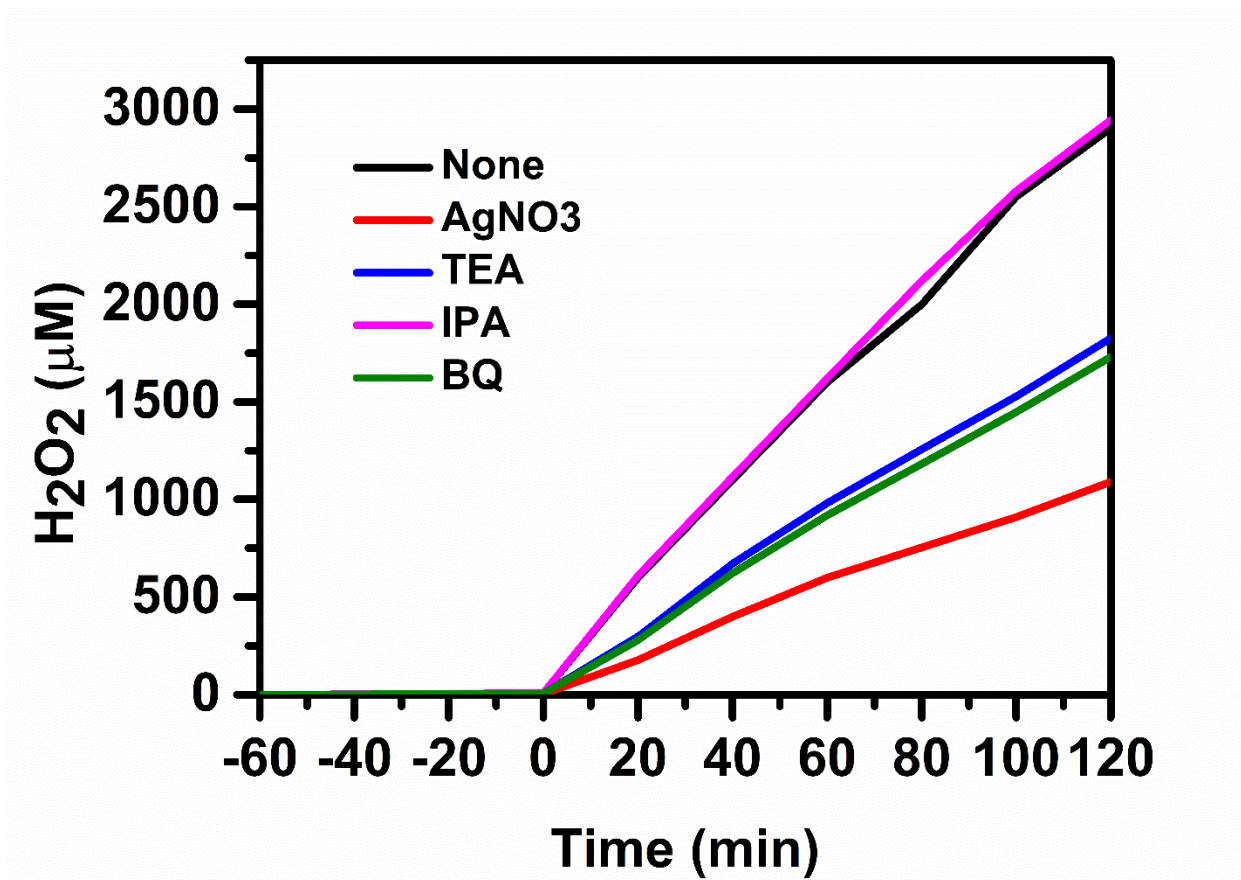


**Fig. S5.** $H_2O_2$ production with addition of scavengers.

12. Absorbance curves of NBT
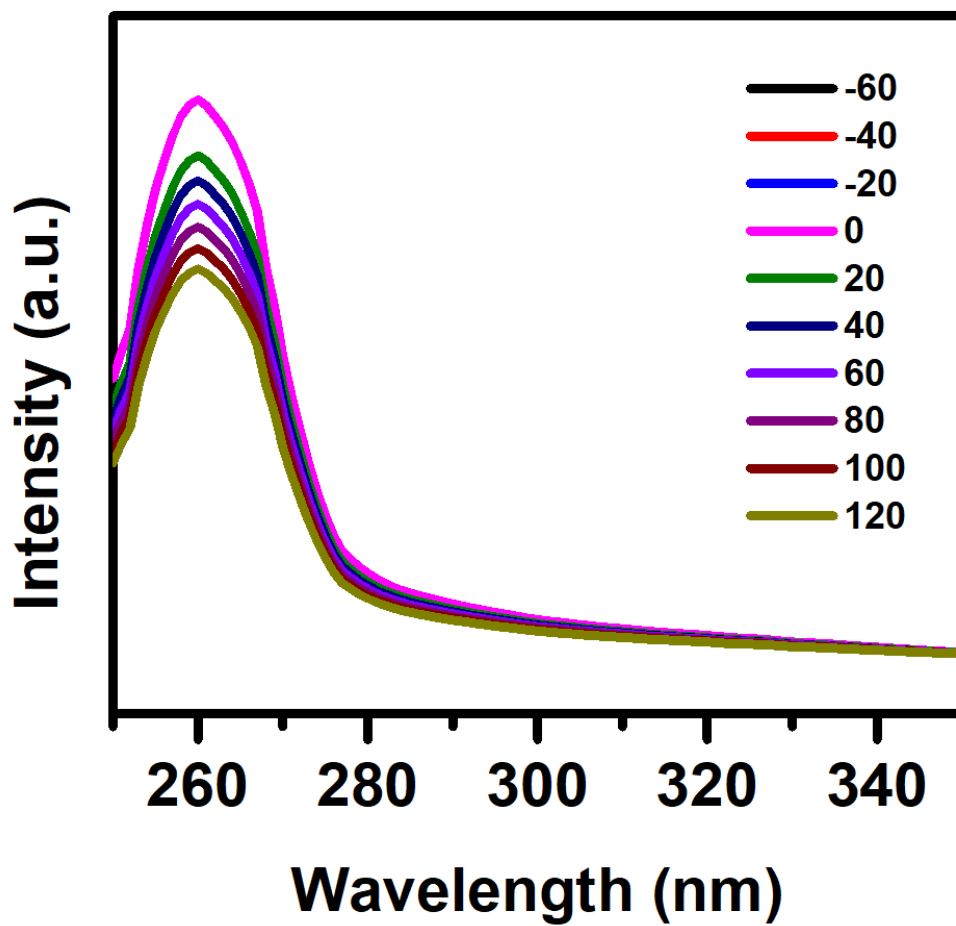


**Fig. S6.** Absorbance curves of NBT.

13. Mott Schottky calculations

Mott-Schottky equation is as follows:

$$\frac{1}{C^2} = \frac{2}{\varepsilon \varepsilon_0 A^2 e N_d} \left(V - V_{fb} - \frac{k_B T}{e}\right)$$

where  C is the capacitance;

$\varepsilon$ is the dielectric constant;

$\varepsilon_0$ is the permittivity of free space;

A is the surface area of electrode;

e is the elementary charge;

$N_d$ is the charge carrier density;

V is the applied potential;

$V_{fb}$ is the flat band potential;

$k_B$ is the Boltzmann constant;

T is the absolute temperature.

**Table S8.** Mott Schottky data.

| Sample | $V_{fb}$(V) | $N_d$ |
|---|---|---|
| CBO | 1.05 | 5.67E+17 |
| $MoS_2$ | 0.12 | 4.33E+18 |
| CBO@$MoS_2$ | 1.04 | 2.52E+18 |

14. Electron transfer number calculation

Koutecký–Levich (K-L) equation is used to calculate the electron transfer number (n):

$$\frac{1}{i} = \frac{1}{B\sqrt{\omega}} + \frac{1}{i_k} \qquad\qquad \text{(viii)}$$

$$B = 0.62\, n\, F D_o^{\frac{2}{3}}\, \gamma^{\frac{-1}{6}}\, C_o \qquad\qquad \text{(ix)}$$

where $i$ is measured current density;

$i_k$ is the kinetic current density;

$n$ is the electron transfer number;

$\omega$ is rotation speed (rad s$^{-1}$): $\omega = 2\pi N$, N is the linear rotation speed;

$F = 96485$ C mol$^{-1}$;

$C_o$ is the concentration of O$_2$ in bulk ($C_o = 8.43 \times 10^{-7}$ mol cm$^{-3}$),

$D_o$ is the diffusion coefficient of O$_2$ in the electrolyte at 298 K ($D_o = 1.43 \times 10^{-5}$ cm$^2$ s$^{-1}$),

$\gamma$ is the kinematic viscosity of the electrolyte ($\gamma = 0.0112$ cm$^2$ s$^{-1}$).

**Table S9**. Electron transfer number at various potentials.

| Potential (V vs RHE) | 0.7 | 0.6 | 0.55 | 0.5 | 0.45 | 0.4 | 0.35 |
|---|---|---|---|---|---|---|---|
| Transfer number | 2.12 | 2.14 | 2.12 | 2.21 | 2.31 | 2.27 | 2.35 |

15. STH efficiency.

Half-cell solar to hydrogen (HC-STH) efficiency can be calculated using the equation below:

$$HC - STH\ (\%) = \frac{|J_{ph}|[V_{bias} - V_{H^+/H_2}]}{J_{in}} \times 100$$

where $J_{ph}$ = photocurrent density (mAcm$^{-2}$) at measured bias.

$V_{bias}$ = applied bias potential w.r.t RHE.

$V_{H^+/H_2}$ = standard potential for hydrogen evolution reaction i.e., 0 V vs RHE.

$J_{in}$ = power density of light illumination, 100 mWcm$^{-2}$.
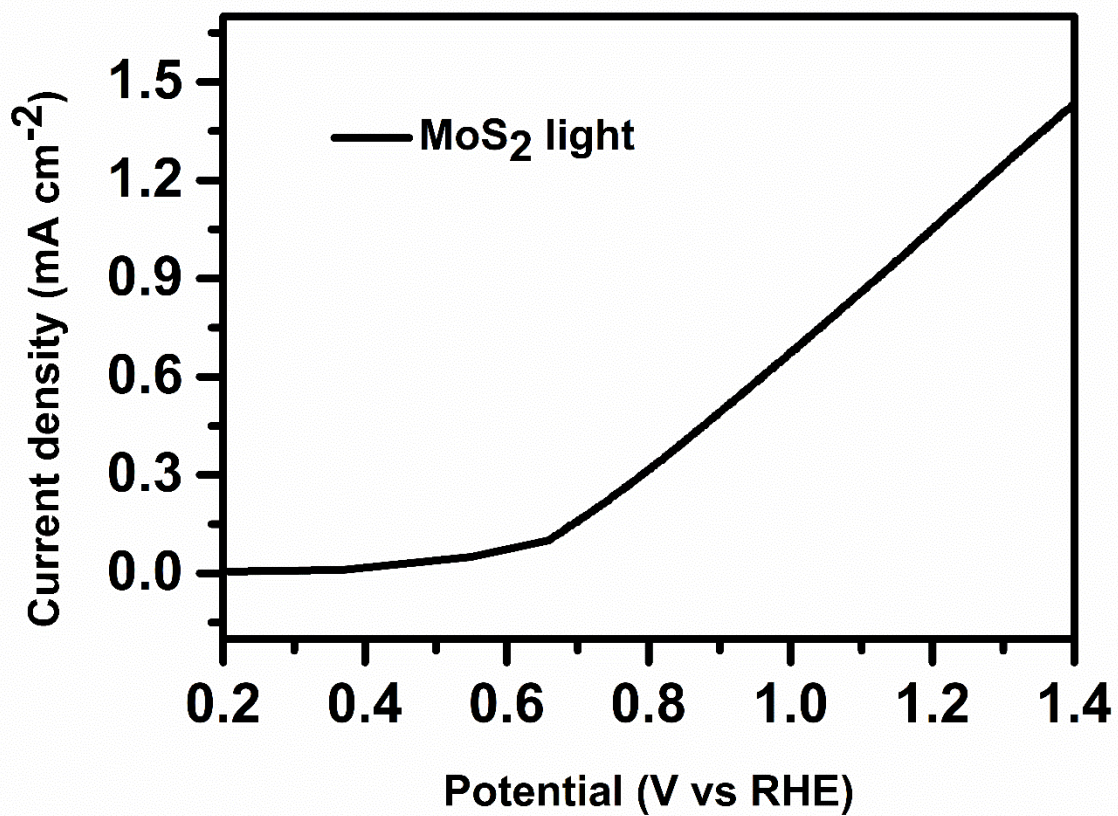
**Fig. S7.** LSV curve of MoS$_2$ for OER.

## 17. References:

[1] Y. Shiraishi, S. Kanazawa, Y. Kofuji, H. Sakamoto, S. Ichikawa, S. Tanaka, T. Hirai, Sunlight-driven hydrogen peroxide production from water and molecular oxygen by metal-free photocatalysts, Angew. Chem. Int. Ed Engl. 53 (2014) 13454–13459. https://doi.org/10.1002/anie.201407938.

[2] T. Baran, S. Wojtyła, A. Minguzzi, S. Rondinini, A. Vertova, Achieving efficient $H_2O_2$ production by a visible-light absorbing, highly stable photosensitized $TiO_2$, Appl. Catal. B Environ. 244 (2019) 303–312. https://doi.org/10.1016/j.apcatb.2018.11.044.

[3] R. Ma, L. Wang, H. Wang, Z. Liu, M. Xing, L. Zhu, X. Meng, F.-S. Xiao, Solid acids accelerate the photocatalytic hydrogen peroxide synthesis over a hybrid catalyst of titania nanotube with carbon dot, Appl. Catal. B Environ. 244 (2019) 594–603. https://doi.org/10.1016/j.apcatb.2018.11.087.

[4] Y. Peng, L. Wang, Y. Liu, H. Chen, J. Lei, J. Zhang, Visible-Light-Driven Photocatalytic $H_2O_2$ Production on g-$C_3N_4$ Loaded with CoP as a Noble Metal Free Cocatalyst, Eur. J. Inorg. Chem. 2017 (2017) 4797–4802. https://doi.org/10.1002/ejic.201700930.

[5] Preparation of N-vacancy-doped g-$C_3N_4$ with outstanding photocatalytic $H_2O_2$ production ability by dielectric barrier discharge plasma treatment, (n.d.). https://www.cjcatal.com/EN/abstract/abstract22410.shtml (accessed May 1, 2023).

[6] J. Xu, Z. Chen, H. Zhang, G. Lin, H. Lin, X. Wang, J. Long, $Cd_3(C_3N_3S_3)_2$ coordination polymer/graphene nanoarchitectures for enhanced photocatalytic $H_2O_2$ production under visible light, Sci. Bull. 62 (2017) 610–618. https://doi.org/10.1016/j.scib.2017.04.013.

[7] Y. Isaka, Y. Kawase, Y. Kuwahara, K. Mori, H. Yamashita, Two-Phase System Utilizing Hydrophobic Metal–Organic Frameworks (MOFs) for Photocatalytic Synthesis of Hydrogen Peroxide, Angew. Chem. Int. Ed. 58 (2019) 5402–5406. https://doi.org/10.1002/anie.201901961.

[8] Y. Lu, Y. Huang, Y. Zhang, T. Huang, H. Li, J. Cao, W. Ho, Effects of $H_2O_2$ generation over visible light-responsive Bi/$Bi_2O_2$−x$CO_3$ nanosheets on their photocatalytic NOx removal performance, Chem. Eng. J. 363 (2019) 374–382. https://doi.org/10.1016/j.cej.2019.01.172.

[9] J.H. Lee, H. Cho, S.O. Park, J.M. Hwang, Y. Hong, P. Sharma, W.C. Jeon, Y. Cho, C. Yang, S.K. Kwak, H.R. Moon, J.-W. Jang, High performance $H_2O_2$ production achieved by sulfur-doped carbon on CdS photocatalyst via inhibiting reverse $H_2O_2$ decomposition, Appl. Catal. B Environ. 284 (2021) 119690. https://doi.org/10.1016/j.apcatb.2020.119690.

[10] H. Song, L. Wei, L. Chen, H. Zhang, J. Su, Photocatalytic Production of Hydrogen Peroxide over Modified Semiconductor Materials: A Minireview, Top. Catal. 63 (2020) 895–912. https://doi.org/10.1007/s11244-020-01317-9.

[11] Y. Yang, Q. Wang, X. Zhang, X. Deng, Y. Guan, M. Wu, L. Liu, J. Wu, T. Yao, Y. Yin, Photocatalytic generation of $H_2O_2$ over a Z-scheme $Fe_2O_3$@C@1T/2H-$MoS_2$ heterostructured catalyst for high-performance Fenton reaction, J. Mater. Chem. A. 11 (2023) 1991–2001. https://doi.org/10.1039/D2TA08145H.